Journal of Physics and Chemistry of Solids 77 (2015) 85–91

Contents lists available at ScienceDirect

Journal of Physics and Chemistry of Solids

journal homepage: www.elsevier.com/locate/jpcs

Vibrational and thermodynamic properties of orthorhombic $CaSnO_3$ from DFT and DFPT calculations

E. Moreira [a], C.A. Barboza [b,*], E.L. Albuquerque [b], U.L. Fulco [b], J.M. Henriques [c], A.I. Araújo [c]

[a] Departamento de Ciências Exatas, Tecnológicas e Humanas, Universidade Federal Rural do Semi-Árido, Campus Angicos, 59515-000 Angicos-RN, Brazil
[b] Departamento de Biofísica e Farmacologia, Universidade Federal do Rio Grande do Norte, 59072-970 Natal-RN, Brazil
[c] Centro de Educação e Saúde, Universidade Federal de Campina Grande, Campus Cuité, 58175-000 Cuité-PB, Brazil

ARTICLE INFO

Article history:
Received 16 July 2014
Received in revised form
9 September 2014
Accepted 14 September 2014
Available online 30 October 2014

Keywords:
A. Ab initio calculations
B. Raman spectroscopy
C. Phonon spectrum
D. Thermodynamics properties

ABSTRACT

Density functional theory (DFT) and density functional perturbation theory (DFPT) calculations were used to investigate the vibrational and thermodynamic properties of orthorhombic stannate $CaSnO_3$ compound. Our approach was based on the generalized gradient approximation with dispersion correction (GGA+D), considering the norm-conserved pseudopotentials. The phonon dispersion relation as well as theoretical peaks of the infrared (IR) and Raman spectrum in the frequency range of 100–800 cm^{-1} was analyzed and assigned. The thermodynamic potentials and the specific heat at constant volume of the $CaSnO_3$ compound are also calculated, whose dependence with the temperature are discussed.

1. Introduction

In recent years, perovskite alkaline earth stannate compounds, such as $BaSnO_3$, $CaSnO_3$ and $SrSnO_3$, have been widely investigated [1–3]. The main reason behind this interest lies in their interesting dielectric properties, leading to several potential applications as transparent conducting oxides (TCOs), which are employed in the fabrication of transparent electrodes for photovoltaic cell and organic light-emitting diodes [4–8]. Besides, they can be used as electronic/chemical devices such as chemical sensors [9], stable capacitors [10], water photoelectrolysis systems [11,12], flat panel displays [13], antistatic coating [14], lithium batteries and humidity sensor [15]. The perovskite structures of these compounds are either cubic ($BaSnO_3$) or orthorhombic ($CaSnO_3$ and $SrSnO_3$).

In particular, the stannate compound $CaSnO_3$ has also attracted considerable attention in the geophysics community since it is an isostructural analog to $(Mg,Fe)SiO_3$ perovskite, the most abundant silicate on Earth [16]. An understanding of the isostructured $CaSnO_3$ would be important due to its suitability to conduct experiments at lower pressure regarding the phase transition from the perovskite to the postperovskite structure in $MgSiO_3$ compound [17].

Research works on $CaSnO_3$ perovskites in the scientific literature were devoted, in the last decades, mainly to some technological points of interest. Some of these issues are the following:

(a) high capacity anode material for Li-ion batteries [18];
(b) phosphorescent material for traffic signs, interior decoration, and light sources ($CaSnO_3$:Tb has afterglow of 4 h after irradiation by 254 nm light [19], and the $CaSnO_3$:Eu^{3+} emission spectra is dominated by red $^5D_o \rightarrow {}^7F_2$ transition at 614 nm [20]);
(c) capacitor component, since sintered $CaSnO_3$ samples are invariant over several decades of frequency [21];

A recent investigation employing Raman spectroscopy was performed to study the behavior of vibrational modes of $CaSnO_3$ perovskite under high pressure [22]. It was found that $CaSnO_3$ remains a $GdFeO_3$-type perovskite up to 26 GPa. Note that the assignment of Raman peaks in this study was carried out by comparing them with the Raman modes of $CaZrO_3$ and other isostructural Ca-bearing perovskites, since no detailed lattice dynamic studies of $CaSnO_3$ are available to date.

Although these technological issues are quite important, it is instructive to perform further systematic investigation on the fundamental physical properties of $CaSnO_3$, like its structural, electronic, dielectric, lattice vibration and thermodynamic properties. To fill this gap, it is the aim of this work to investigate the vibrational and thermodynamic properties (such as the infrared and Raman spectra, the heat capacity, Debye temperature, enthalpy, entropy and free energy) of orthorhombic $CaSnO_3$ perovskites. Our theoretical/computational approach is based on quantum chemistry calculations, using the density functional theory (DFT) together with the density functional perturbation theory

* Corresponding author. Tel.:+ 55 84 3215 3419.
E-mail address: ca.barbo3a@gmail.com (C.A. Barboza).

http://dx.doi.org/10.1016/j.jpcs.2014.09.016
0022-3697/

(DFPT) within the generalized gradient approximation with dispersion correction (GGA+D).

The plan of this paper is as follows: in Section 2 we present our computer calculation methodology. Section 3 deals with the main results regarding the physical properties of orthorhombic $CaSnO_3$, including its geometry optimization, a detailed calculation of the Raman and infrared (IR) active modes, the dielectric permittivities and polarizabilities, phonon spectrum and phonon density of states (DOS). Its thermodynamic properties are also depicted in this section. The conclusions are presented in Section 4.

2. Methodology

The DFT calculations for perovskite $CaSnO_3$ were performed using the crystallographic data obtained from Zhao et al. [23] and Mountstevens et al. [24]. Fig. 1 shows some views of the crystal (top) with the tilting of SnO_6 octahedra (bottom). The experimental lattice parameters are $a=5.5142$ Å, $b=5.6620$ Å, and $c=7.8814$ Å, and the space group is *Pbnm* (62), according to Table 1. Atomic coordinates for orthorhombic $CaSnO_3$ are shown in Table 2.

The CASTEP code was used to carry out the DFT calculations [25,26]. The orthorhombic $CaSnO_3$ structure, optimized through the GGA-PBE approximation, was used to perform the density functional perturbation theory (DFPT)-linear response calculations [27] in order to obtain its vibrational properties. Within the generalized gradient approximation (GGA), which is more stringent than the local density approximation (LDA), we have used the Perdew–Burke–Ernzerhof [28] parametrization. The PBE functional leads to results close to the ones obtained by using the PW91 functional [29] within the Tkatchenko–Scheffler (TS) method [30] for the dispersion correction scheme (DFT+D) to describe the van der Waals interactions. We have also used pseudopotentials to replace the core electrons in each atomic species. The norm-conserved pseudopotentials [31], generated using the OPIUM code [32], were adopted in the GGA calculations following the same scheme of previous works [2,33,34]. The electronic valence configurations for each atomic species were: Ca – $3s^2 3p^6 4s^2$, Sn – $5s^2 5p^2$, and O – $2s^2 2p^4$. A Monkhorst–Pack [35] $3 \times 3 \times 2$ sampling was used to evaluate all integrals in reciprocal space, which is more than enough to give a well converged electronic structure.

Lattice parameters, angles and atomic positions were optimized by seeking a total minimum energy for the $CaSnO_3$ unit cell. In order to perform the geometry optimization, the following convergence thresholds were considered for successive self-consistent steps: total energy change smaller than 0.5×10^{-5} eV/atom, maximum force over each atom below 0.01 eV/Å, pressure smaller than 0.02 GPa, and maximum allowed atomic positions displacements not exceeding 0.5×10^{-3} Å. The Broyden–Fletcher–Goldfarb–Shannon (BFGS) minimizer [36] was employed to carry out the unit cell optimization. In the BFGS scheme a starting Hessian is recursively updated. For each self-consistent field step, the electronic minimization parameters were total energy/atom convergence tolerance

Table 1
Lattice parameters for orthorhombic $CaSnO_3$ crystal calculated within the GGA-PBE approach by using the norm-conserving pseudopotential. For the sake of comparison, we have also included similar results obtained from Ref. [1], as well as the experimental data (EXP.) from Ref. [24]. Lengths (*a*, *b*, *c*) are in Å and volumes (*V*) in $Å^3$.

E–C potential	*a*	*b*	*c*	*V*
GGA	5.3872 (−2.3%)	5.4424 (−3.8%)	7.6495 (−2.9%)	224.2815 (−8.8%)
GGA [1]	5.6086 (+1.7%)	5.7978 (+2.3%)	8.0452 (+2.1%)	261.6101 (+6.0%)
EXP. [24]	5.5142	5.6620	7.8814	246.1354

Table 2
Internal atomic coordinates (*u*, *v*, and *w*) for orthorhombic $CaSnO_3$ according with the GGA-PBE calculations, together with experimental values from Ref.[24].

Atom		*u*	*v*	*w*
Ca	GGA	−0.4929	0.5341	0.25
	EXP.	−0.0141(3)	0.0506	0.25
Sn	GGA	0.0	0.5	0.5
	EXP.	0.0	0.5	0.0
O1	GGA	0.0709	0.4824	0.25
	EXP.	0.0997(2)	0.04644(2)	0.25
O2	GGA	0.7128	0.2861	0.0370
	EXP.	0.6988(1)	0.2982(1)	0.0517(1)

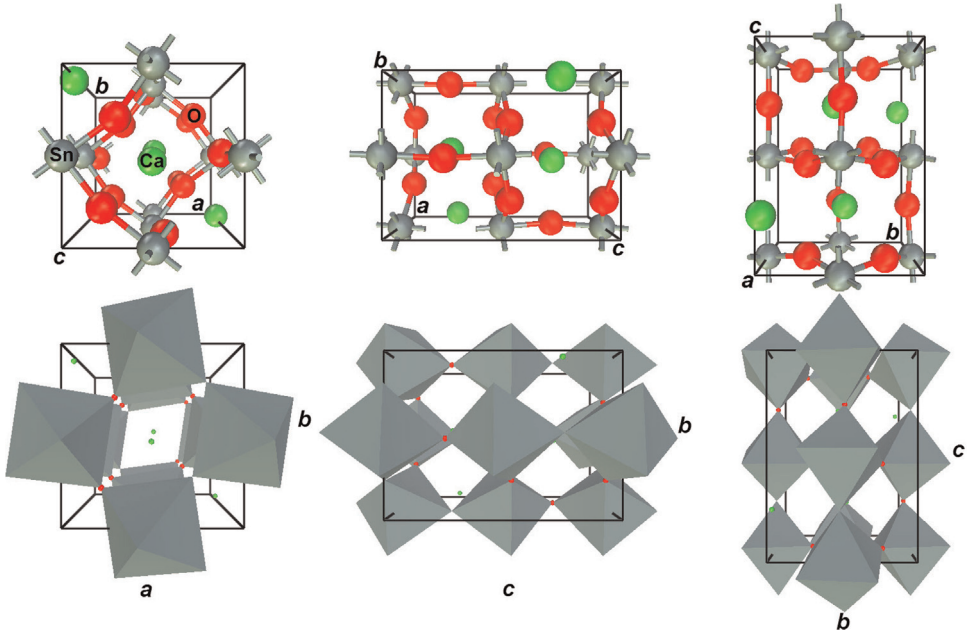

Fig. 1. The structure of orthorhombic $CaSnO_3$. Top: different views of the unit cell and atomic labels. Bottom: tilted SnO_6 octahedra in the orthorhombic $CaSnO_3$ unit cell.

of 0.5×10^{-6} eV, eigen-energy threshold of 0.1562×10^{-6} eV at most, and a convergence window of 3 cycles. A plane-wave basis set was adopted to represent the Kohn–Sham orbitals, with cutoff energy chosen, after convergence studies, to be 880 eV when using the norm-conserved pseudopotentials. The quality of this basis set is kept fixed as the unit cell volume varies during geometry optimization. After obtaining the optimized unit cell and atomic positions, the infrared and Raman spectra were evaluated for the optimized GGA unit cell as well as the frequencies of active modes, together with the calculated dielectric permittivity and polarizability tensors, by following the same scheme described in previous works [33–35,37]. Furthermore, the phonon calculations were carried out within the harmonic approximation, using the density functional perturbation theory (DFPT) calculation, or linear response formalism [27,38], to determine its dispersion and density of states. We are aware that DFPT calculations in CASTEP have some restrictions, like the phonon calculations must be performed with fixed occupancies (insulators) and without spin polarization by using only norm conserving pseudopotentials [39].

3. Results and discussion

3.1. Geometry optimization

The calculated structural parameters for orthorhombic $CaSnO_3$ are shown in Table 1, together with similar results for orthorhombic $CaSnO_3$ obtained from Ref. [1], for the sake of comparison. Experimental data for $CaSnO_3$ from Mountstevens et al. [24] are presented as well. Fractionary atomic coordinates for orthorhombic $CaSnO_3$ are shown in Table 2.

The GGA exchange-correlation functionals tend to underestimate the strength of interatomic forces, leading to larger lattice parameters. Notwithstanding that, the GGA estimations for $CaSnO_3$ using norm-conserved pseudopotentials generated by the OPIUM code have a good agreement with available X-ray data, with differences between -2.3% (a) and -2.9% (c). Earlier work [1], in which the GGA data for orthorhombic $CaSnO_3$ were obtained using ultrasoft pseudopotentials, have differences being at least $+1.7\%$ larger for the a parameter.

3.2. Infrared and Raman spectra, dielectric permittivities and polarizabilities

The GGA-optimized structure was used to perform the density functional perturbation theory (DFPT)-linear response calculations in order to obtain the $CaSnO_3$ vibrational properties, providing an analytical way to obtain the second derivative of the total energy with respect to some external disturbance, such as the ionic position, the external electric field or a change in the unit cell vectors. As a result, we can determine some physical properties like the phonon spectra, the dielectric response or the elastic constants.

The geometry optimization criteria were more stringent than the one used for the LDA calculations. The convergence thresholds were total energy convergence tolerance smaller than 5×10^{-6} eV/atom, maximum ionic force smaller than 1×10^{-2} eV/Å, maximum ionic displacement tolerance of 5×10^{-4} Å, and maximum stress component smaller than 2×10^{-2} GPa. For the self-consistent field calculations, the convergence criteria took into account a total energy per atom variation smaller than 5×10^{-7} eV, and $CaSnO_3$ variation smaller than 0.1562×10^{-6} eV.

The infrared absorption intensities are related to the dynamical (Hessian) matrix and to the Born effective charges, also known as atomic polarizability tensors (ATP) [27], and can be obtained by calculating the phonons at the Γ point. The Raman spectrum, on the other hand, is widely used to study the vibrational, rotational, and low-frequency modes in a system, being based on the Raman shift of inelastic scattering of monochromatic light [40]. The interaction of the light with atomic vibrations results in the energy of incident photons being shifted up or down, the energy shift being dependent on the spacial derivatives of the macroscopic polarization [41]. The IR and Raman spectra of the orthorhombic $CaSnO_3$ are shown in Figs. 2 and 3, respectively. Table 3 presents the predicted normal modes with the respective irreducible representations and the assignment of IR and Raman active modes. The B_{1u}, B_{2u} and B_{3u} modes are IR active, the A_g, B_{1g}, B_{2g} and B_{3g} are Raman active, whereas the A_u is spectroscopically inactive (silent mode).

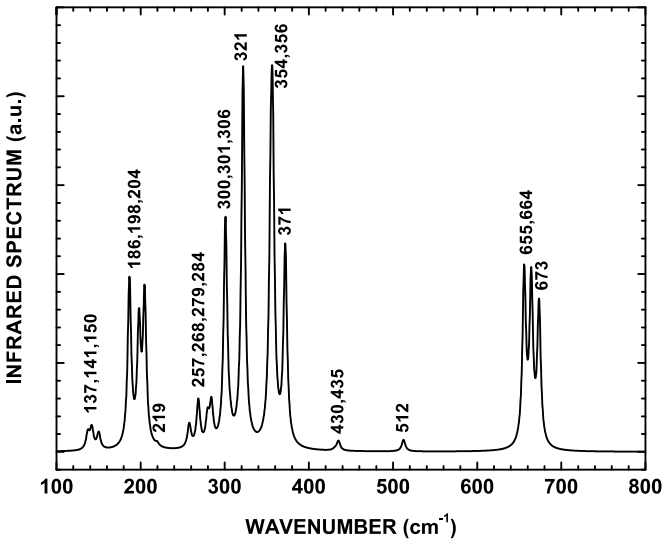

Fig. 2. Infrared spectra of orthorhombic $CaSnO_3$ in the 100–800 cm^{-1} range. The numbers correspond to the normal modes shown in Table 3.

Orthorhombic $CaSnO_3$ has 57 normal modes at $\mathbf{k} = 0$, with 25 IR active modes, $\Gamma_{IR} = 9B_{1u} + 7B_{2u} + 9B_{3u}$. In accordance with some reports [2,42,43], the vibrations of the stannate group (SnO_3^{2-}) produce high intensity infrared absorption bands in the ranges of 300–400 and 600–700 cm^{-1} [42], with the stretching vibration of the Sn–O bond being located at about 674 cm^{-1} [44]. Looking at

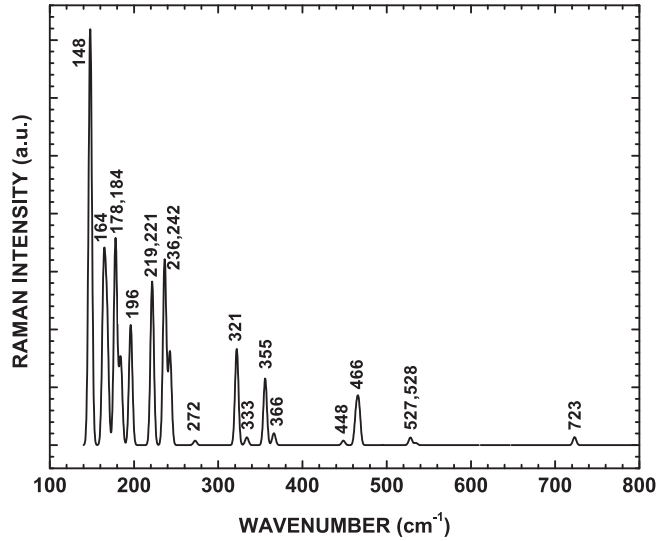

Fig. 3. Raman spectra of orthorhombic $CaSnO_3$ in the 100–800 cm^{-1} range. The numbers correspond to the normal modes shown in Table 3.

Table 3
Normal modes of orthorhombic $CaSnO_3$ at $\mathbf{k}=0$. Irreducible representations (Irreps) are indicated, as well as the IR and Raman active modes.

N	k (cm^{-1})	Irrep	IR	Raman	N	ν (cm^{-1})	Irrep	IR	Raman
1	127.8	A_u	N	N	30	320.9	B_{3u}	Y	N
2	137.2	B_{2u}	Y	N	31	321.9	A_g	N	Y
3	141.9	B_{3u}	Y	N	32	333.9	B_{3g}	N	Y
4	148.0	A_g	N	Y	33	354.9	B_{1u}	Y	N
5	150.2	B_{1u}	Y	N	34	355.0	A_u	N	N
6	164.1	A_g	N	Y	35	355.7	B_{1g}	N	Y
7	167.9	B_{2g}	N	Y	36	357.0	B_{2u}	Y	N
8	170.6	A_u	N	N	37	366.0	B_{2g}	N	Y
9	178.0	B_{2g}	N	Y	38	372.1	B_{1u}	Y	N
10	178.9	A_u	N	N	39	430.6	B_{1u}	Y	N
11	184.1	B_{3g}	N	Y	40	435.0	B_{3u}	Y	N
12	186.6	B_{2u}	Y	N	41	448.5	B_{2g}	N	Y
13	196.0	B_{3g}	N	Y	42	463.7	B_{3g}	N	Y
14	198.2	B_{1u}	Y	N	43	466.9	A_g	N	Y
15	204.7	B_{3u}	Y	N	44	495.4	B_{2g}	N	Y
16	219.6	B_{3u}	Y	N	45	512.4	B_{3u}	Y	N
17	221.5	B_{2g}	N	Y	46	527.5	B_{1g}	N	Y
18	236.4	A_g	N	Y	47	528.3	B_{3g}	N	Y
19	242.6	B_{1g}	N	Y	48	534.5	A_g	N	Y
20	257.8	B_{1u}	Y	N	49	648.4	A_u	N	N
21	268.5	B_{2u}	Y	N	50	649.6	B_{2u}	Y	N
22	269.8	A_u	N	N	51	655.7	B_{3u}	Y	N
23	272.5	A_g	N	Y	52	662.4	A_u	N	N
24	279.5	A_u	N	N	53	664.2	B_{2u}	Y	N
25	279.6	B_{1u}	Y	N	54	673.5	B_{1u}	Y	N
26	283.9	B_{3u}	Y	N	55	723.0	B_{1g}	N	Y
27	300.7	B_{2u}	Y	N	56	760.6	B_{2g}	N	Y
28	301.3	B_{1u}	Y	N	57	789.3	B_{3g}	N	Y
29	306.6	B_{3u}	Y	N					

Fig. 2, the most intense IR absorption peaks occur at 321.88 cm^{-1} (indicated as 321), the band near 356.92 cm^{-1} (indicated as 356) looks a little more intense in comparison, but their individual peaks are less intense than the peak at 321.88 cm^{-1}, a mode with irreducible representation B_{3u} which is assigned to a O–Sn–O scissors movement along the *b*-axis and O–Sn–O bending along the *a*-axis, within the *ab*-plane, as in Ref. [2]. The second most intense peak appears at 356.92 cm^{-1} (indicated as 356) being assigned to a O–Sn–O bending movement in the *ab*-plane with irreducible representation B_{2u}, while the third most intense one occurs at 371.92 cm^{-1} (indicated as 371), corresponding to O–Sn–O bending movement in the *ab*-plane with irreducible representation B_{1u}. Two close peaks at 300.59 and 301.15 cm^{-1} produce a very intense absorption band, and correspond to a O–Sn–O bending movement in the *ab*-plane with irreducible representation B_{2u}, and an asymmetrical O–Sn–O bending movement in the *ab*-plane with irreducible representation B_{1u}. Smaller peaks can be seen at 137.25 cm^{-1} related with the movement of Ca ions up and down (and SnO_6 tetrahedra up and down) along the *b*-axis. At 673.53 cm^{-1}, an intense absorption peak is also noted, being assigned to an asymmetrical stretching of the O–Sn–O bond, like those in Ref. [42].

Fig. 3 presents the calculated Raman scattering spectrum. There are 24 Raman active modes at $\mathbf{k}=0$ with $\Gamma_{Raman} = 7A_g + 4B_{1g} + 7B_{2g} + 6B_{3g}$, close to theoretical calculation [43] and experimental results [45–47]. In the 0–200 cm^{-1} range, the most intense peak at 148 cm^{-1} (149.6 [44], and 145 cm^{-1}[45]) is assigned to an A_g mode corresponding to the scissors movement of O–Sn–O groups along the *a*-axis within the *ab*-plane. In the 200–400 cm^{-1} range, the intense peak at 242.68 cm^{-1} (241.6 [44], 247 [45], 246 [46] and 245.3 cm^{-1} [47]) is related to a B_{1g} mode corresponding to the scissors movement of O–Sn–O groups along the *b*-axis and a symmetrical stretching of the Sn–O–Sn bond. In the 400–600 cm^{-1} range, the intense peak at 466.9 cm^{-1} (467.6 cm^{-1} [44]) is assigned to an A_g mode corresponding to the scissors movement of Sn–O–Sn groups along the *a*-axis. In the 600–800 cm^{-1} range, the intense peak at 723 cm^{-1} (720.3 [44], 699 [46], and 700.9 cm^{-1} [47]) is related to a B_{1g} mode corresponding to a symmetrical stretching of the O–Sn–O bond.

The optical permittivity tensor components calculated for orthorhombic $CaSnO_3$ at $\omega=0$ ($\omega=\infty$) are ϵ_{xx} = 14.47879 (3.60939), ϵ_{yy} = 15.44036 (3.59623), ϵ_{zz} = 16.36083 (3.56652), $\epsilon_{xy}=\epsilon_{xz}=\epsilon_{yz}=0$ (0).

On the other hand, the polarizability tensor (in units of $Å^3$) for $\omega=0$ – static ($\omega=\infty$- optical) has the following components: p_{xx} = 240.56622 (46.57177), p_{yy} = 257.72807 (46.33680), p_{zz}= 274.15641 (45.80654), $p_{xy}=p_{xz}=p_{yz}=0$ (0).

3.3. Phonon spectrum and phonon density of states

The phonon's properties can be determined by using an harmonic approximation, whose description of the lattice vibrations, according to Ref. [30], yields for its strength

$$D_{\mu\nu}(R-R') = \left[\frac{\partial^2 E}{\partial u_\mu(R)\partial u_\nu(R')}\right]_{u=0}, \quad (1)$$

where *u* refers to the displacement of a given atom and *E* is the total energy in the harmonic approximation. Each atomic displacement is described in the form of plane waves, i.e.

$$u(\mathbf{R}, t) = \varepsilon \exp\left[i[\mathbf{k}.\mathbf{R} - \omega(\mathbf{k})t]\right] \quad (2)$$

where the polarization vector of each mode (ε) is an eigenvector (with a 3N dimension) of the eigenvalue problem:

$$M\omega(\mathbf{k})^2\varepsilon = D(\mathbf{k})\varepsilon. \quad (3)$$

The phonon density of states (or vibrational density of states) for a given band *n* is defined as

$$N_n(\omega) = \int \frac{d\mathbf{k}}{4\pi^3}\delta\left[\omega - \omega_n(\mathbf{k})\right], \quad (4)$$

where $\omega_n(\mathbf{k})$ describes the dispersion of a given band, the integral being calculated over the first Brillouin zone.

To perform the phonon's spectrum calculations we have used the CASTEP code within the DFT formalism, in combination with the GGA approximation within the TS method [30] for the dispersion correction scheme (DFT+D) in order to determine the van der Waals interactions. Here we have adopted the norm-conserving pseudopotentials to replace the core electrons in each atomic species, all of them generated using the OPIUM code.

For each self-consistent field step, the electronic minimization parameters were total energy/atom convergence tolerance of 0.5×10^{-6} eV, eigen-energy threshold of 0.1562×10^{-6} eV at most, and a convergence window of 3 cycles. A plane-wave basis set was adopted to represent the Kohn–Sham orbitals, with cutoff energy chosen, after convergence studies, to be 880 eV.

Regarding the phonon parameters we have considered the phonon convergence tolerance of 0.1×10^{-4} eV/Å and the band convergence tolerance of 0.1×10^{-8} eV. We have included the LO (longitudinal optical)/TO (transverse optical) phonon splitting term and adopted the acoustic phonon sum role in the reciprocal space.

Fig. 4 depicts the phonon dispersion curves along some high-symmetry points in the Brillouin zone (left panel) and the total density of phonon states mode (right panel) for orthorhombic

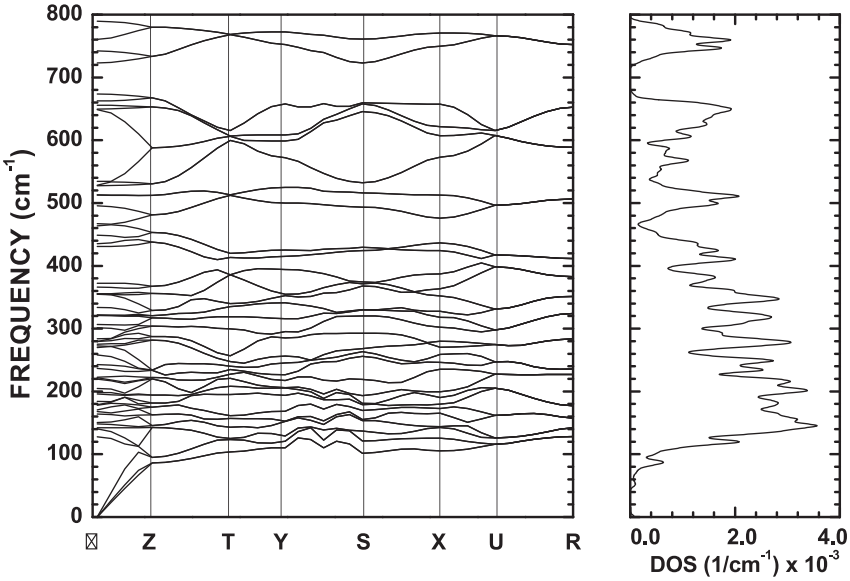

Fig. 4. Phonon dispersion curves (left panel) and the density of phonon states (DOS) mode/cm^{-1} (right panel) of orthorhombic $CaSnO_3$ in the frequency range from 0 to 800 cm^{-1}, calculated using the GGA-PBE-OPIUM exchange-correlation functionals.

$CaSnO_3$ in the frequency range from 0 to 800 cm^{-1}. It indicates that the phonon structure is stable since throughout the Brillouin zone all phonon frequencies are positive. The main features of the dispersion curves is the presence of three well defined frequency regions corresponding to

(a) a region from 0 to 520 cm^{-1} with contribution, mostly, of SnO_6 tetrahedra, O–Sn–O bending and Sn–O–Sn scissoring movements;
(b) after a gap of 13 cm^{-1}, approximately, a second region from 530 cm^{-1} to 640 cm^{-1}, which has a dominant contribution from a Sn–O–Sn scissors movement;
(c) a third region up to 800 cm^{-1}, after a gap of 100 cm^{-1}, corresponding to a stretching mode of O–Sn–O bonds.

In the left panel, depicting the phonon density of states spectrum, the peaks (gaps) are related to the corresponding modes for each region.

3.4. Thermodynamic properties

The thermodynamic properties of materials are closely related to their vibrational properties, yielding not only a guidance for insights about their atomic lattice behavior, but also providing essential information for technological applications. It is well known that heat capacities increase with increasing temperature, due to the phonon thermal vibrations. At high temperatures ($T > 400$ K), the anharmonic effect is suppressed, and the constant volume heat capacity C_V approaches the Dulong–Petit classical limit (for monoatomic solids $C_V = 3Nk_B$, where N is the number of atoms per cell and k_B is Boltzmann's constant). In the low temperature limit, C_V is proportional to T^3, while at intermediate temperatures its temperature dependence is ruled by detailed atomic lattice vibrations, whose dependence may be determined from experiments.

Phonon calculations from DFPT can be used to compute the thermodynamic potentials' enthalpy (H), free energy (F) and the temperature times the entropy term $TS = U - F$ (U being the internal energy), as well as the lattice heat capacity (C_V) as a function of the temperature. The CASTEP software yields the total electronic energy at zero Kelvin, whose vibrational contributions to the thermodynamic properties are evaluated to compute H, F, TS and C_V at finite temperatures.

The temperature dependence of the thermodynamic potentials can be found in Ref. [27]. For the enthalpy H we have

$$H(T) = E_{tot} + E_{zp} + \int \frac{\hbar\omega}{\exp\left(\frac{\hbar\omega}{k_B T}\right) - 1} N(\omega)\, d\omega, \tag{5}$$

where E_{zp} is the zero point vibrational energy, k_B is Boltzmann's constant, $\hbar$ is Planck's constant, and $N(\omega)$ is the phonon density of states.

The vibrational contribution to the free energy, F, is

$$F(T) = E_{tot} + E_{zp} + k_B T \int N(\omega) \ln\left[1 - \exp\left(-\frac{\hbar\omega}{k_B T}\right)\right] d\omega, \tag{6}$$

while for the temperature times the entropy term, $TS = U - F$, we have

$$TS(T) = k_B T \left\{ \int \frac{\frac{\hbar\omega}{k_B T}}{\exp\left(\frac{\hbar\omega}{k_B T}\right) - 1} N(\omega) d\omega - \int N(\omega) \left[1 - \exp\left(-\frac{\hbar\omega}{k_B T}\right)\right] d\omega \right\}. \tag{7}$$

We have preferred to use $TS(T)$ instead of $S(T)$ to emphasize the contribution of the thermodynamic potentials.

On the other hand, the heat capacity at constant volume (C_V), as a function of T, has been calculated at zero pressure. The lattice

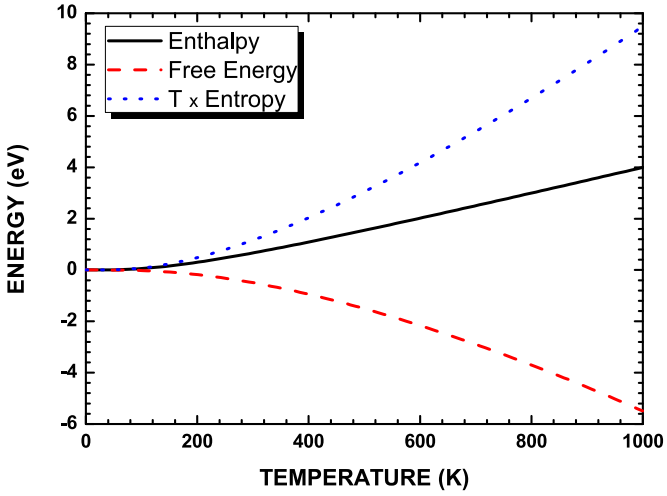

Fig. 5. Profiles of the calculated thermodynamic potentials' enthalpy (black: solid line), free energy (red: medium dashed line) and $T\times$ entropy (blue: small dashed line), as a function of the temperature, for orthorhombic $CaSnO_3$. (For interpretation of the references to color in this figure caption, the reader is referred to the web version of this paper.)

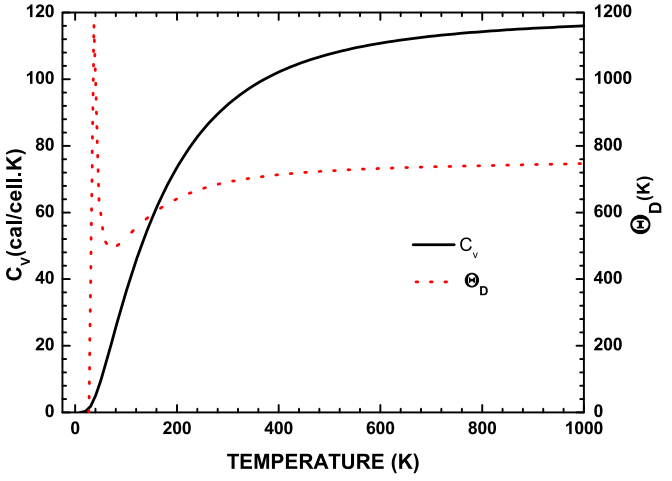

Fig. 6. Constant volume heat capacity C_V, as given by Eq. (8), as a function of the temperature (in K). The red dotted line, using the right-hand side scale, depicts the temperature dependence of the Debye temperature $\Theta_D(T)$. (For interpretation of the references to color in this figure caption, the reader is referred to the web version of this paper.)

contribution to the C_V is [27]

$$C_V(T) = k_B \int \frac{\left(\frac{\hbar\omega}{kT}\right)^2 \exp\left(\frac{\hbar\omega}{kT}\right)}{\left[\exp\left(\frac{\hbar\omega}{kT}\right) - 1\right]^2} N(\omega)\, d\omega. \tag{8}$$

A common representation of the experimental data on the heat capacity is based on the comparison of the actual heat capacity, as defined by Eq. (8), to those predicted by the Debye model, as given by [48]

$$C_V^{Debye}(T) = 9Nk_B\left(\frac{T}{\Theta_D}\right)^3 \int_0^{x_D} \frac{x^4 e^x}{(e^x - 1)^2}\, dx, \tag{9}$$

where N is the number of atoms per cell. Also $x_D = \Theta_D/T$, with Θ_D being the so-called Debye temperature. This leads to the concept of the temperature dependent $\Theta_D(T)$, whose profile can be obtained by substituting the specific heat $C_V(T)$ found in Eq. (8) into Eq. (9).

Fig. 5 shows the profiles of the calculated thermodynamic potentials' enthalpy, free energy and the temperature times the entropy term, $TS = U - F$, as a function of the temperature (in K), for orthorhombic $CaSnO_3$. From there one can see that the enthalpy (black: solid line) has an almost linear behavior as a function of the temperature, while the free energy (red: medium dashed line) slightly decreases up to 400 K, assuming after that a linear behavior as the temperature increases. The term TS (blue: small dashed line), as expected, increases exponentially as a function of the temperature.

Fig. 6 depicts the constant volume heat capacity C_V, as given by Eq. (8), as a function of the temperature (in K). It is easy to see that the heat capacity C_V increases as the temperature increases, reaching the Dulong–Petit limit at around 600 K. Using the right-hand side scale of Fig. 6, we have also shown the behavior of the temperature dependent $\Theta_D(T)$ (red dotted line).

These results can be compared with the experimental data, or used to predict the phase stability for different structural modifications.

4. Conclusions

In this work, we have obtained the geometry optimization, vibrational properties, dielectric permittivities and polarizability tensors, phonon spectrum and density of states, besides the thermodynamic properties of the orthorhombic $CaSnO_3$ perovskites using quantum chemistry first-principles calculations.

The structural parameters of $CaSnO_3$, calculated after geometry optimization, show a good agreement with the experimental data, with a difference of 3.8% in the worst case (b-axis). The GGA exchange-correlation functionals tend to underestimate the strength of the interatomic forces, leading to larger lattice parameters. Notwithstanding that the GGA estimations for $CaSnO_3$, using norm-conserved pseudopotentials generated by the OPIUM code, have a good agreement with known X-ray data.

We have also obtained the infrared and Raman spectra using the GGA-optimized structure to perform density functional perturbation theory (DFPT)-linear response calculations in order to obtain its vibrational properties. The vibrations of the stannate group produce high intensity infrared absorption bands in the ranges of 300–400 and 600–700 cm^{-1} within the most intense IR absorption peaks. These vibrations correspond to the frequency peak position at 321.88 cm^{-1} with irreducible representation B_{3u}, which is assigned to a O–Sn–O scissors movement along the b-axis and O–Sn–O bending along the a-axis, within the ab-plane, according to the experimental results. The calculated Raman spectrum exhibits a good agreement with experimental data, with the most intense peak at 148 cm^{-1} assigned to an A_g mode corresponding to the scissors movement of O–Sn–O groups along the a-axis within the ab-plane.

Regarding the phonon spectrum, the main feature of its dispersion curves is the presence of three well defined frequency regions, as far as the atomic arrangements' contributions are concerned. It is clear that no imaginary phonon frequency exists in the whole Brillouin zone, indicating the dynamical stability of our system. These results can be compared with the experimental data, for example heat capacity measurements, or used to predict either a phase stability of different structural modifications or a phase transition.

Finally, the thermodynamic properties of the $CaSnO_3$ compound, here measured by its specific heat capacity and Debye temperature, are illustrated in Figs. 5 and 6 depicting their profiles with the temperature.

Acknowledgments

This work was partially financed by the Brazilian Research Agencies CAPES (RedeNanoBioTec) and CNPq (INCT-Nano(Bio) Simes, Casadinho/Procad and PNPD).

References

[1] J.M. Henriques, E.W.S. Caetano, V.N. Freire, J.A.P. da Costa, E.L. Albuquerque, J. Phys.: Condens. Matter 19 (2007) 106214.
[2] E. Moreira, J.M. Henriques, D.L. Azevedo, E.W.S. Caetano, V.N. Freire, E. L. Albuquerque, J. Solid State Chem. 184 (2011) 921.
[3] X. Jiang, F.L. Wong, M.K. Fung, S.T. Lee, Appl. Phys. Lett. 83 (2003) 1875.
[4] I. Hamberg, C.G. Granqvist, J. Appl. Phys. 60 (1986) R123.
[5] T. Minami, Semicond. Sci. Technol. 20 (2005) S35.
[6] Y. Furubayashi, T. Hitosugi, Y. Yamamoto, K. Inaba, G. Kinoda, Y. Hirose, T. Shimada, T. Hasegawa, Appl. Phys. Lett. 86 (2005) 252101.
[7] J. Cui, A. Wang, N.L. Edleman, J. Ni, P. Lee, N.R. Armstrong, T.J. Marks, Adv. Mater. 13 (2001) 1476.
[8] H. Kim, C.M. Gilmore, J.S. Horwitz, A. Piqu, H. Murata, G.P. Kushto, R. Schlaf, Z. H. Kafafi, D.B. Chrisey, Appl. Phys. Lett. 76 (2000) 259.
[9] W. Lu, S. Jiang, D. Zhou, S. Gong, Sensors Actuators 80 (2000) 35.
[10] X.Y. Wie, X. Yao, Mater. Sci. Eng. B 137 (2007) 184.
[11] W.F. Zhang, J. Tang, J. Ye, Chem. Phys. Lett. 418 (2006) 174.
[12] B. Bellal, B. Hadjarab, A. Bouguelia, M. Trari, Theor. Exp. Chem. 45 (2009) 172.
[13] H. Mizoguchi, H.W. Eng, P.M. Woodward, Inorg. Chem. 43 (2004) 1667.
[14] N. Al-Dahoudi, H. Bisht, C. Gbbert, T. Krajewski, M.A. Aegerter, Thin Solid Films 392 (2001) 299.
[15] Z. Lu, J. Liu, J. Tang, Y. Li, Inorg. Chem. Commun. 7 (2004) 731.
[16] G.R. Helffrich, B.J. Wood, Nature 412 (2001) 501.
[17] A. Yangthaisong, Chin. Phys. Lett. 30 (2013) 077101-1.
[18] N. Sharma, K.M. Shaju, G.V. Subb Rao, B.V.R. Chowdari, Electrochem. Commun. 4 (2002) 947.
[19] Z. Liu, Y. Liu, Mater. Chem. Phys. 93 (2005) 129.
[20] Z. Lu, L. Chen, Y. Tang, Y. Li, J. Alloys Compd. 387 (2005) L1.
[21] A.-M. Azad, L.L. Shyan, M.A. Alim, J. Mater. Sci. 34 (1999) 1175.
[22] J. Kung, Y.J. Lin, C.M. Lin, J. Chem. Phys. 135 (2011) 224507.
[23] J. Zhao, N.L. Ross, R.J. Angel, Phys. Chem. Miner. 31 (2004) 299.
[24] E.H. Mountstevens, J.P. Attfield, S.A.T. Redfern, J. Phys.: Condens. Matter 15 (2005) 8315.
[25] P. Hohenberg, W. Kohn, Phys. Rev. B 136 (1964) 864.
[26] W. Kohn, L.J. Sham, Phys. Rev. A 140 (1965) 1133.
[27] S. Baroni, S. de Gironcoli, A. dal Corso, P. Giannozzi, Rev. Mod. Phys. 73 (2001) 515.
[28] J.P. Perdew, K. Burke, M. Ernzerhof, Phys. Rev. Lett. 77 (1996) 3865.
[29] J.P. Perdew, J.A. Chevary, S.H. Vosko, K.A. Jackson, M.R. Pederson, D.J. Singh, C. Fiolhais, Phys. Rev. B 46 (1992) 6671.
[30] A. Tkatchenko, M. Scheffler, Phys. Rev. Lett. 102 (2009) 073005.
[31] J.S. Lin, A. Qteish, M.C. Payne, V. Heine, Phys. Rev. B 47 (1993) 4174.
[32] A.M. Rappe, K.M. Rabe, E. Kaxiras, J.D. Joannopoulos, Phys. Rev. B 41 (1990) 1227.
[33] P.D. Sesion Jr, J.M. Henriques, C.A. Barboza, E.L. Albuquerque, V.N. Freire, E.W. S. Caetano, J. Phys.: Condens. Matter 22 (2010) 435801.
[34] E. Moreira, J.M. Henriques, D.L. Azevedo, E.W.S. Caetano, V.N. Freire, U.L. Fulco, E.L. Albuquerque, J. Appl. Phys. 112 (2012) 043703.
[35] H.J. Monkhorst, J.D. Pack, Phys. Rev. B 13 (1976) 5188.
[36] B.G. Pfrommer, M. Cote, S.G. Louie, M.L. Cohen, J. Comput. Phys. 131 (1997) 133.
[37] J.E.F.S. Rodrigues, E. Moreira, D.M. Bezerra, A.P. Maciel, C.W.A. Paschoal, Mater. Res. Bull. 48 (2013) 3298.
[38] M. Babiker, D.R. Tilley, E.L. Albuquerque, C.E.T. Gonçalves da Silva, J. Phys. C: Solid State Phys. 18 (1985) 1269.
[39] Accelrys, Materials Studio CASTEP, Accelrys, San Diego, 2009.
[40] M. Babiker, D.R. Tilley, E.L. Albuquerque, J. Phys. C: Solid State Phys. 18 (1985) 1285.
[41] D. Porezag, M.R. Pederson, Phys. Rev. B 54 (1996) 7830.
[42] M.C.F. Alves, S.C. Souza, M.R.S. Silva, E.C. Paris, S.J.G. Lima, R.M. Gomes, E. Longo, A.G. de Souza, I.M. Garcia dos Santos, J. Therm. Anal. Calorim. 97 (2009) 179.
[43] M. Licheron, G. Jouan, E. Husson, J. Eur. Ceram. Soc. 17 (1997) 1453.
[44] A. Yangthaisong, Chin. Phys. Lett. 30 (2013) 077101.
[45] M. Tarrida, H. Larguem, M. Madon, Phys. Chem. Miner. 36 (2009) 403.
[46] P. McMillan, N. Ross, Phys. Chem. Miner. 16 (1988) 21.
[47] J. Kung, Y.J. Lin, C.M. Lin, J. Chem. Phys. 135 (2011) 224507.
[48] N.W. Ashcroft, N.D. Mermin, Solid State Physics, Saunders College, Philadelphia, 1976.